Published in final edited form as:

Conf Proc IEEE Eng Med Biol Soc. 2016 August ; 2016: 5757–5760. doi:10.1109/EMBC.2016.7592035.

Polyimide-Based Magnetic Microactuators for Biofouling Removal

Qi Yang[1,2,5,6], **Tran Nguyen**[1,5,6], **Chunan Liu**[1,2,5,6], **Jacob Miller**[3,4,5], **Jeffrey F. Rhoads**[3,4,5], **Jacqueline Linnes**[1,6], and **Hyowon Lee**[1,5,6]

[1]Weldon School of Biomedical Engineering, Purdue University, West Lafayette, USA

[2]School of Electrical Engineering, Purdue University, West Lafayette, USA

[3]School of Mechanical Engineering, Purdue University, West Lafayette, USA

[4]Ray W. Herrick Laboratories, Purdue University, West Lafayette, USA

[5]Birck Nanotechnology Center, Purdue University, West Lafayette, USA

[6]Center for Implantable Devices, Purdue University, West Lafayette, USA

Abstract

Here we report on the development of novel polyimide-based flexible magnetic actuators for improving hydrocephalus shunts. The static and dynamic mechanical responses of the thin-film magnetic microdevices were quantitatively measured. The bacteria-removing capabilities of the microfabricated devices were also evaluated. Although additional evaluations are necessary, the preliminary results show promising potential for combatting bacteria-induced biofouling. Lastly, the thin-film microdevices are integrated into a single-pore silicone catheter to demonstrate a proof-of-concept, MEMS-enabled self-clearing, smart catheter.

Keywords

Magnetic microactuators; thin-film device; implantable microdevice; BioMEMS; hydrocephalus; biofouling

I. Introduction

Implantable medical devices, such as catheters and biosensors, often suffer from functional degradation over the course of their lifetime due to biofouling. For devices that manage chronic disease, such as hydrocephalus, a sudden failure can lead to a catastrophic outcome for the patient. Hydrocephalus is a neurological disorder that is characterized by an abnormal accumulation of cerebrospinal fluid (CSF) in the brain, often due to an imbalance between the generation and absorption of CSF. It is commonly observed in children with approximately 1-2 newborns diagnosed for every 1000 in the US [1], [2]. Unfortunately, there is no cure for this debilitating disease. The gold standard for treatment of hydrocephalus is the implantation of a shunt system to divert excess CSF from the brain to another part of the body [3]. However, shunt systems are notorious for their extremely high failure rate of more than 40% within 1 year and up to 85% within 10 years of implantation

[4], [5]. A large portion of this high failure rate can be attributed to biofouling-related obstruction and infection [4], [6].

To combat biofouling *in situ* without the risk of additional neurosurgical intervention, we have previously proposed to use microfabricated magnetic actuators for removing bioaccumulation on ventricular catheters. A magnetic microactuator is ideal for such applications due to its simplicity (i.e., no integrated circuits or power source). Although the cellular removal capabilities [7], durability [8], and magnetic resonance imaging compatibility [9] of these devices have been demonstrated, they have only been fabricated on rigid silicon substrate thus far, which complicates integration into a flexible silicone catheter body. To facilitate the integration of microfabricated devices into silicone-based catheters, we designed, fabricated, and tested a novel thin-film polymer-based microactuator in an effort to create a self-clearing smart catheter. In this work, we demonstrate a novel process flow to create polyimide-based magnetic microactuators. We report static and dynamic mechanical responses of these devices, and evaluate their bacteria clearing capabilities. Furthermore, we demonstrate the first proof-of-concept integrated flexible magnetic microactuators in a silicone-based implantable catheter.

II. Device Design and Fabrication

A. Device Structure

Our thin film devices use a single cantilever beam structure. The structural plate is patterned out of a uniform polyimide layer. Polyimide is chosen as the structural material because of its excellent chemical resistance, biocompatibility and good mechanical properties [10]. The microdevice features the same design previously reported in [8]. At the tip of the cantilever beam, an electroplated nickel magnet covers the surface of a circular structural plate. The diameter of the structural plate is chosen to be 900 μm, which is slightly smaller than the pore size of a ventricular catheter. In the presence of a magnetic field, the magnetic element can apply a moment on the flexure, causing out-of-plane deflection. The large amplitude out-of-plane deflection produced in this manner can mechanically remove biofouling. Assuming that the torsional load on the polyimide cantilever is a concentrated on tip, the relationship between the applied magnetic field and the resulting deflection angle ϕ can be described by: [11], [12]

$$\phi = V_m M H \sin\left(\frac{\pi}{2} - \phi\right) / k_{\text{beam}}$$

with cantilever stiffness k_{beam}, magnet volume V_m, magnetization M, and applied magnetic field H. We experimentally determined 12 μm as the optimal thickness for reasonable stiffness and overall structural strength. Using the fixed thickness, we tested 6 variations that differ in beam length and width as shown in Table 1.

B. Fabrication

Figure 1 illustrates the overall process flow. Starting from a single-side polished 100 mm silicon wafer (Silicon Quest, San Jose, CA), 500 nm of silicon dioxide (SiO_2) was first deposited as a release layer using plasma enhanced chemical vapor deposition (Axic, Milpitas, CA). On top of the oxide layer, polyimide (PI-2525, HD Microsystem, Parlin, NJ) was spin coated at 1500 rpm and soft baked on hotplate (130 °C and 150 °C successively for 30 s each). An adhesion promoter (VM652, HD Microsystem, Parlin, NJ) was used before the application of polyimide to ensure good adhesion. The sample was then cured using a nitrogen oven with the manufacturer specified heating sequence.

Next, a 20 nm chromium adhesion layer and 50 nm gold conduction layer were deposited using an electron beam evaporator (Varian). The pattern of the electroplated nickel was defined by 25 μm thick photoresist (AZ9260, Microchemicals, Germany). The nickel ferromagnetic element was electroplated in 2 L plating solution containing 1 M nickel sulfamate, 0.4 M boric acid, and 10 g sodium dodecyl sulfate at 60 °C. 10 μm thick nickel was deposited in 38 min using the current density of 10 mA/cm^2.

The structural plate was defined by oxygen plasma etching in an Advanced Oxide Etcher (Surface Technology System, Newport, United Kingdom). An oxygen and argon gas mixture (7:1) was used under 600 W RF coil and 20 W platen power. The polyimide thickness was then verified using Alpha-Step IQ surface profiler (KLA-Tencor, Milpitas, CA) after oxygen plasma etching. To release the sample, the wafer was placed in 6:1 buffered oxide etchant for approximately 40 hours. After release, 500 nm of Parylene C was conformally coated (PDS2010, Specialty Coating System, Indianapolis, IN) to improve biocompatibility.

III. Mechanical Responses

After the samples were fabricated, their mechanical response was characterized. Static deflection, frequency response in air and the frequency response in deionized water were measured to obtain optimal operating actuation amplitude and frequency.

A. Static Response

To characterize the static mechanical response of the fabricated magnetic microactuator, the angular deflection as a function of the applied magnetic field strength was measured for each device. The magnetic field was generated using a custom-made iron core electromagnet magnet. The magnetic field strength was measured using a gaussmeter (8010 Gauss/ Telsameter, Pacific Scientific, Chandler, AZ) as a function of applied current. The individual device structure, as shown in Fig. 2a, was aligned and gently placed on a 5 mm thick PDMS mold with 2 mm diameter through-holes for structural support. PDMS was then placed on top of the electromagnet under a digital microscope (KH8700, Hirox, Hackensack, NJ). The top edge of nickel magnet and the base of the cantilever, shown in Fig. 2c, were focused upon and their vertical positions were recorded. The difference between the two points was then converted into deflection angle using device geometry. Results obtained from each device type is presented in Fig. 3. The results indicate that approximately 15–25 kA/m of

magnetic field strength can result in fairly large deflections (> 45°), and this will serve as a general guide to what magnetic field strength is needed to use to actuate the device *in vivo*.

B. Dynamic Response

The dynamic response of the polyimide-based magnetic microactuators were measured in air and in deionized water to identify the resonant frequency at which the device actuates with high energy efficiency. Another electromagnet with a 6-inch-long ferrite 77 core (Fair-Rite, Wallkill, NY) was made for measuring the dynamic responses because of its high relative permeability and excellent frequency response. The device was placed on a PDMS fixture on top of the electromagnet in the same manner as with the DC measurements. A scanning laser Doppler vibrometer (MSA-400, Polytec, Waldbronn, Germany) was used to measure out-of-plane velocity at a series of points across the actuator surface. The electromagnet was driven with a swept sine excitation generated by the MSA-400 system. The fast Fourier transform algorithm was applied to the time series velocity data, and frequency-domain integration was used to develop a spatially-averaged displacement spectrum for the device. A linear approximation of the impedance of the magnet was used to estimate the current applied. The H1 frequency response estimator was then calculated, giving the best linear estimate of the relation between current and displacement from 1.25 to 1200 Hz with a 1.25 Hz resolution. A plot of the magnitude of the H1 frequency response estimator is shown in Fig 4. The frequency at which peak amplitude occurred in air was recorded below in Table 1.

IV. Bacteria Removal

A. Material and Procedure

The device was placed inside a sterile test tube with *Escherichia Coli* in a 5 ml Lysogeny Broth and incubated overnight in a shaker incubator (250 rpm) at 37 °C. Following incubation, the tube was taken out and placed in room temperature for another two hours to facilitate the adhesion of *E. coli* onto the device. Three groups of devices were tested: control, non-actuated, actuated in a cross-sectional comparison. For the control condition, devices were taken from the incubation tube, immediately stained (T = 0) using a Live/Dead Bacteria Viability Kit (Thermo Fisher Scientific) and imaged under an inverted fluorescent microscope (Axio Observer Z1, Carl Zeiss). The images were taken with a 10× objective using a 17-Alexa Fluor 488 reflector (live/green) and a 20-HE Rhodmanie reflector (dead/red). The non-actuated devices were placed in the 1X PBS solution for 20 min without applying magnetic field, then stained with fluorescent dyes, and imaged under the microscope. The actuated devices were subjected to 26.5 kA/m of magnetic field at 100 Hz, then stained and imaged. The time elapsed due to the actuation and imaging was approximately 45 min.

B. Results

Images were taken and processed using Fiji software (Lifeline version) [13]. Figure 5 includes images of the device at each experimental conditions. Intensities of the devices in all conditions were calculated and presented as integrated density for region of interest (Fig. 6). We compared the amount of remaining bacteria as evidenced by the integrated density for both live and dead bacteria. There was a large decrease in the amount of live bacteria and

an increase in the amount of dead bacteria after 45 minutes compared to the control, which indicates a progression of bacteria death during the treatment phase of the experiments. The actuated devices had even less live bacteria remain on the surface. However, we noticed further decrease in dead bacteria after the actuation compared to devices without actuation. These results suggest that our devices may be able to remove both live and dead bacteria from its surface.

V. Device Integration

To demonstrate a proof-of-concept MEMS-enabled self-clearing catheter, we integrated our device into a silicone catheter (Fig. 7). Our device structure was slid inside a catheter and aligned to the hole (punctured to represent pore in a central venous access device). The polyimide substrate was rolled to comply with catheter wall curvature and fixed with silicone adhesive.

VI. Conclusion And Dicussions

Here we reported a flexible polyimide-based magnetic microactuator, which exhibits great promise for combating biofouling. The static responses of these microfabricated devices show good agreement with analytical prediction. Additional testing is required to confirm dynamic behaviors of these microactuators, especially in liquid. The flexible nature of the device facilitates integration with catheter as we demonstrated via conceptual catheter-actuator attachment. The manual process is simple and straightforward, however, alignment of an array of devices in multiple-pore catheter design will likely to be more challenging. Next, we will conduct an animal study and implant the integrated catheter device in a porcine model to evaluate shunt biofouling removal *in-situ*.

We also reported on the ability of our magnetic microac-tuator to clear bacteria on the surface of the device. Our preliminary *in vitro* results demonstrated that our device may be capable of removing adherent bacteria grown over its surface via low-frequency, high-amplitude actuation with 20° angular deflection. In future assessments, we will continue to test the clearance capability of our device with a different type of bacteria such as *Staphylococcal aureus* and study long-term biofilm formation and removal.

Acknowledgments

We would like to thank Cook Medical for providing a sample central venous access devices (Model G0664).

References

1. Chi JH, Fullerton HJ, Gupta N. Time trends and demographics of deaths from congenital hydrocephalus in children in the United States: National Center for Health Statistics data, 1979 to 1998. Journal of Neurosurgery. 2005; 103(Pediatrics 2):113–118. [PubMed: 16370275]
2. Simons TD, Hall M, Riva-Cambrin J, Albert JE, Jeffries HE, Lafleur B, Dean JM, Kestle JRW, Network THCR. Infection rates following initial cerebrospinal fluid shunt placement across pediatric hospitals in the United States. Journal of Neuro-surgery Pediatric. 2010; 4(2):156–165.
3. Lutz BR, Venkataraman P, Browd SR. New and improved ways to treat hydrocephalus: Pursuit of a smart shunt. Surgical Neurology International. Jan; 2013 4(Suppl 1):s38–50. [PubMed: 23653889]

4. Browd SR, Ragel BT, Gottfried ON, Kestle JRW. Failure of cerebrospinal fluid shunts: part i: Obstruction and mechanical failure. Pediatric Neurology. Feb; 2006 34(2):83–92. [PubMed: 16458818]
5. Harris CA, McAllister JP. What we should know about the cellular and tissue response causing catheter obstruction in the treatment of hydrocephalus. Neurosurgery. Jun; 2012 70(6):1589–601. discussion 1601–2. [PubMed: 22157548]
6. Drake, JM., Sainte-Rose, C., editors. The Shunt Book. Cambridge: Blackwell Science; 1995.
7. Lee SA, Lee H, Pinney JR, Khialeeva E, Bergsneider M, Judy JW. Development of microfabricated magnetic actuators for removing cellular occlusion. Journal of Micromechanics and Microengineering. 2011; 21(5):054006.
8. Lee H, Kolahi K, Bergsneider M, Judy JW. Mechanical evaluation of unobstructing magnetic microactuators for implantable ventricular catheters. Journal of Microelectromechanical Systems. 2014; 23(4):795–802.
9. Lee H, Xu Q, Shellock FG, Bergsneider M, Judy JW. Evaluation of magnetic resonance imaging issues for implantable microfabricated magnetic actuators. Biomedical Microdevices. 2014; 16(1): 153–161. [PubMed: 24077662]
10. Xiao SY, Che LF, Li XX, Wang YL. a novel fabrication process of mems devices on polyimide flexible substrates. Microelectronic Engineering. 2008; 85(2):452–457.
11. Roark, RJ. Roark's Formulas for Stress and Strain. New York: McGraw-Hill; 1989.
12. Judy JW, Muller RS, Zappe HH. Magnetic Microactuation of Polysilicon Flexure Structures. Journal of Microelectromechanical Systems. 1995; 4(4):162–169.
13. Preibisch S, Saalfeld S, Tomancak P. Globally optimal stitching of tiled 3d microscopic image acquisitions. Bioinformatics. 2009; 25(11):1463–1465. [PubMed: 19346324]

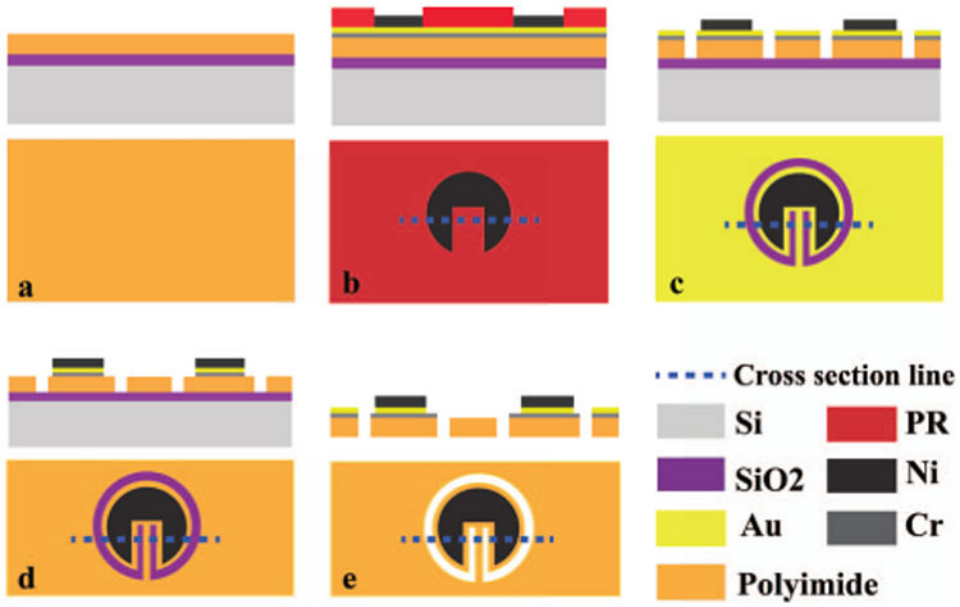

Fig. 1. Fabrication sequence of a polyimide-based magnetic microactuator

(a) Deposition of 500 nm SiO_2 followed by 12 μm polyimide. (b) Evaporation of Cr/Au followed by Ni electroplating. (c) Definition of structural plate patterning. (d) Removal of Cr/Au. (e) Release of the thin-film magnetic microactuator.

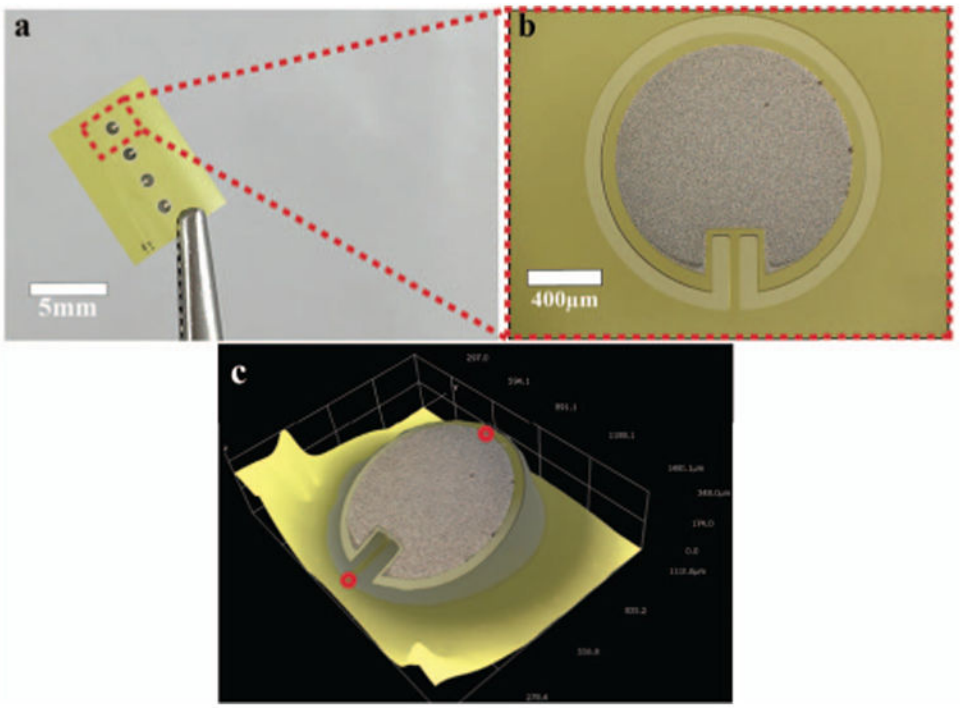

Fig. 2. Photographs of representative fabricated devices

(a) Image of a released magnetic microactuators, prior to Parylene coating. (b) Close-up view of the microactuator (c) 3D optical image of static deflection, the red dots indicate measurement points.

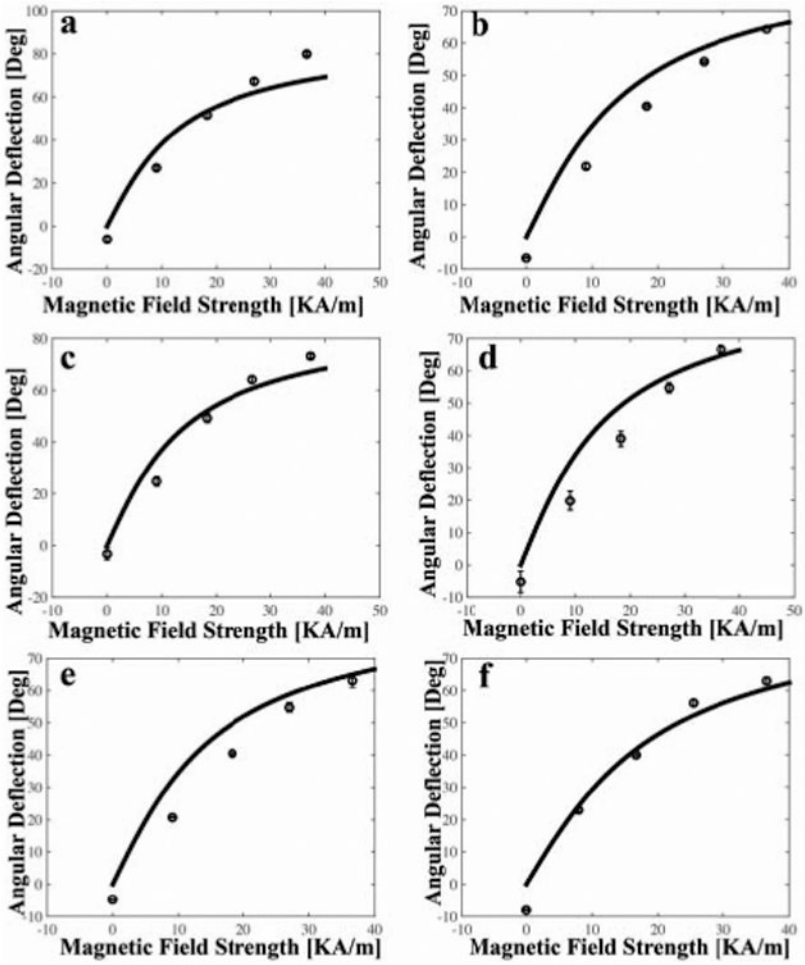

Fig. 3. Static angular deflection

Solid line indicates theoretical prediction, circle represents measured values, a-f correspond to Designs 1-6. The results (n= 2) are expressed as average ± s.d.

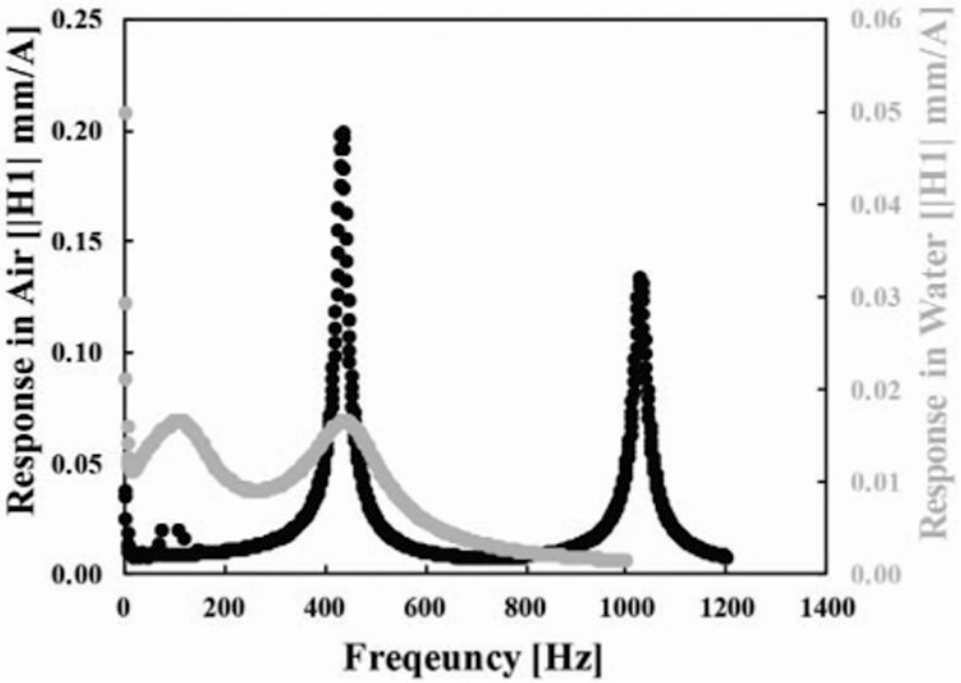

Fig. 4. Comparison of a representative device's magnitude of H1 frequency response estimators between air and water trials

Black circles represent data for air trials, grey axis for deionized water trials, both from Device 5.

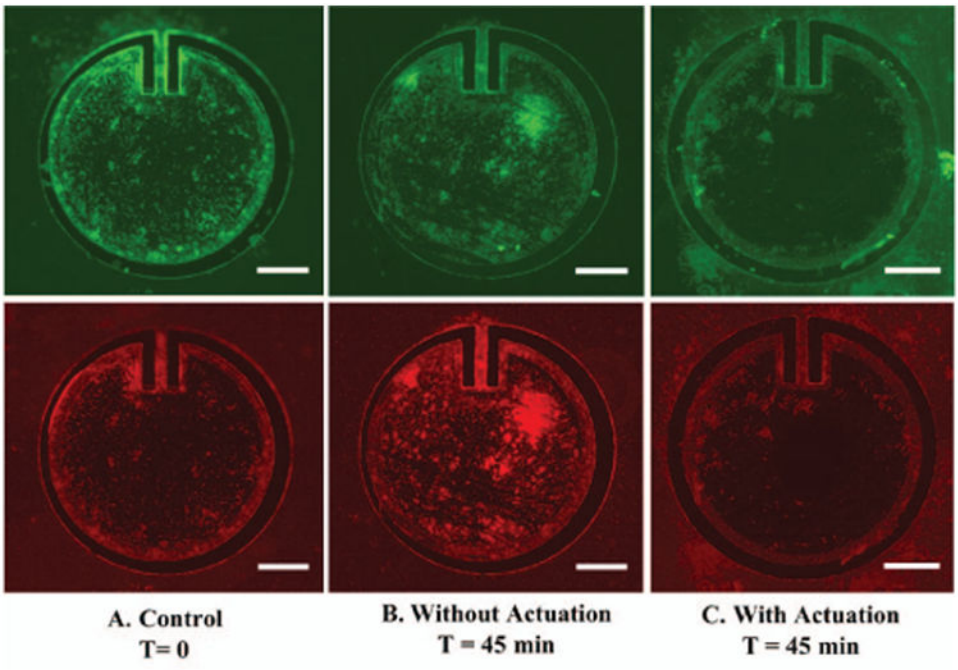

Fig. 5. Bacteria removal capability

A. Initial Bacteria distribution as control at T = 0 min for live and dead bacteria. **B**. Bacteria distribution after 20 min in PBS without actuation at T = 45 min. **C**. Bacteria distribution after 20 min actuation in PBS at T = 45 min. The scale bars = 200 μm.

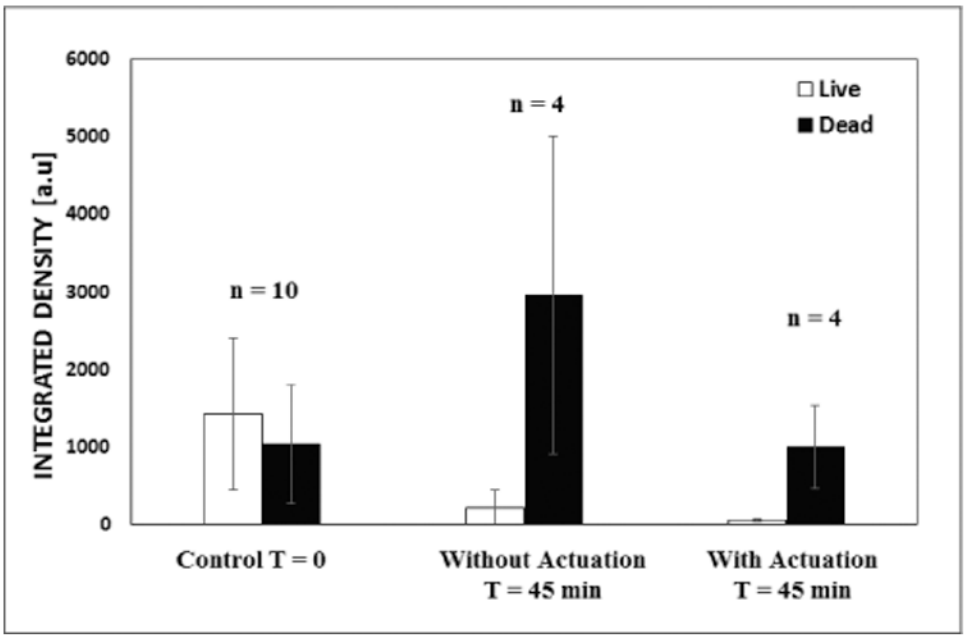

Fig. 6. Integrated density for live and dead bacteria at various experimental conditions

At T = 45 min, there was a large decrease in the amount of live bacteria and an increase in the amount of dead bacteria compare to the control devices. There was a further decrease in the amount of live bacteria and dead bacteria of the actuated devices compared to the devices without actuation at T = 45 min. The results are represented as mean ± standard deviation.

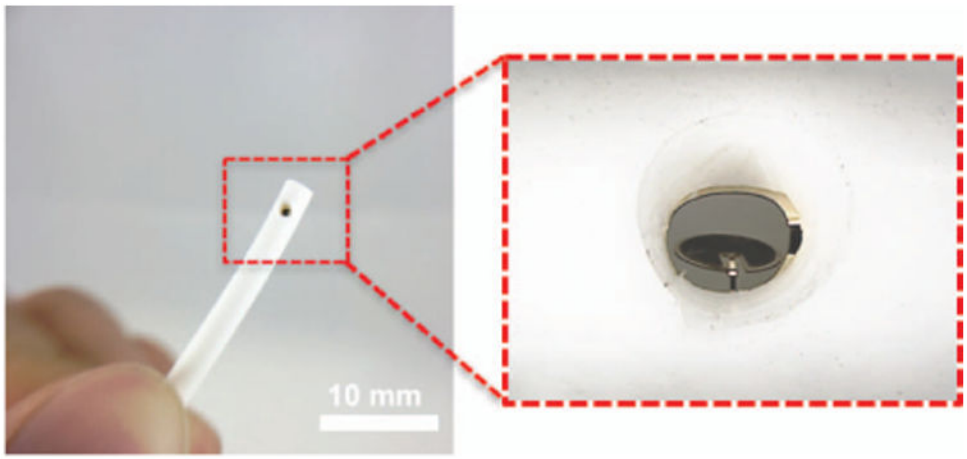

Fig. 7. Device integration into an implantable catheter

The flexible polyimide-based microactuator was rolled into an implantable central venous access catheter (Model G0664)

Table I

Design variation and measured first resonant requency in air

Device [number]	1	2	3	4	5	6
Beam Length [μm]	500	400	400	350	300	250
Beam Width [μm]	49	49	44	44	40	40
First Resonant Frequency [Hz]	384	422	436	460	437	443